

The GALAH survey: Lithium-rich giant stars require multiple formation channels

Sarah L. Martell,^{1,2*} Jeffrey D. Simpson,¹ Adithya G. Balasubramaniam,¹
 Sven Buder,^{2,3} Sanjib Sharma,^{2,4} Marc Hon,¹ Dennis Stello,^{1,2,4} Yuan-Sen Ting,^{3,5,6,7}
 Martin Asplund,^{2,3} Joss Bland-Hawthorn,^{2,4} Gayandhi M. De Silva,^{2,8}
 Ken C. Freeman,³ Michael Hayden,^{2,4} Janez Kos,^{4,9} Geraint F. Lewis,⁴ Karin Lind,^{10,11}
 Daniel B. Zucker,^{2,12} Tomaž Zwitter,⁹ Simon W. Campbell,¹³ Klemen Čotar,⁹
 Jonathan Horner,¹⁴ Benjamin Montet¹ and Rob Wittenmyer¹⁴

¹*School of Physics, UNSW, Sydney, NSW 2052, Australia*

²*Centre of Excellence for Astrophysics in Three Dimensions (ASTRO-3D), Australia*

³*Research School of Astronomy & Astrophysics, Australian National University, ACT 2611, Australia*

⁴*Sydney Institute for Astronomy, School of Physics, A28, The University of Sydney, NSW, 2006, Australia*

⁵*Institute for Advanced Study, Princeton, NJ 08540, USA*

⁶*Department of Astrophysical Sciences, Princeton University, Princeton, NJ 08544, USA*

⁷*Observatories of the Carnegie Institution of Washington, 813 Santa Barbara Street, Pasadena, CA 91101, USA*

⁸*Australian Astronomical Optics, Faculty of Science and Engineering, Macquarie University, Macquarie Park, NSW 2113, Australia*

⁹*Faculty of Mathematics and Physics, University of Ljubljana, Jadranska 19, 1000 Ljubljana, Slovenia*

¹⁰*Max Planck Institute for Astronomy (MPIA), Königstuhl 17, 69117 Heidelberg, Germany*

¹¹*Department of Physics and Astronomy, Uppsala University, Box 517, SE-751 20 Uppsala, Sweden*

¹²*Department of Physics and Astronomy, Macquarie University, Sydney, NSW 2109, Australia*

¹³*School of Physics and Astronomy, Monash University, Clayton, VIC 3800, Australia*

¹⁴*Centre for Astrophysics, University of Southern Queensland, Toowoomba, QLD 4350, Australia*

Accepted XXX. Received YYY; in original form 28th October 2021

ABSTRACT

We investigate the properties of 1306 red giant stars with high photospheric abundances of lithium observed by the GALAH, K2-HERMES and TESS-HERMES surveys, and discuss them in the context of proposed mechanisms for lithium enrichment in giant stars. We confirm that Li-rich giants are rare, making up only 1.1 per cent of our giant star sample. We use GALAH+ DR3 stellar parameters and a Bayesian isochrone analysis to divide the sample into first-ascent red giant branch and red clump stars, and confirm these classifications using asteroseismic data from K2. We find that red clump stars are more than three times as likely to be lithium-rich as red giant branch stars, and the occurrence rate of lithium richness with metallicity is quite different between the two populations. The probability for a rapidly rotating giant to be lithium-rich is distinctly higher as compared to a non rapidly rotating giant, independent of its evolutionary state. There is also a clear correspondence on the red clump between rapid rotation and extreme levels of lithium enrichment. There are almost no stars on the secondary red clump with lithium abundances above the primordial level, indicating a mass dependence in the red clump lithium enrichment mechanism(s). The complex distribution of lithium-rich giants across evolutionary phase, metallicity, rotation rate and mass implies multiple independent mechanisms for producing lithium enrichment.

Key words: stars:abundances – stars:evolution

1 INTRODUCTION

Lithium-rich giants have been a longstanding mystery in stellar evolution (Burbidge et al. 1957; Wallerstein & Conti 1969; Trimble

* Email: s.martell@unsw.edu.au

1975, 1991) since the first such evolved star was discovered by McKellar (1940, 1941). Canonical stellar evolution predicts that a star with approximately solar mass forms with the atmospheric lithium abundance that matches its local interstellar medium, and that abundance is preserved throughout the star’s main sequence lifetime. The structure of solar-mass main sequence stars, with radiative cores and fairly shallow convective envelopes, means that the material in the stellar atmosphere is never exposed to a high enough temperature to destroy the lithium (2.6×10^6 K; Gamow & Landau 1933; Salpeter 1955). Then, in the first dredge-up phase (Iben 1965), which happens as a star evolves from the main sequence toward the red giant branch (RGB), the convective envelope deepens dramatically. First dredge-up transports atmospheric material through the hot stellar interior, which subjects it to proton-capture fusion. This causes a sharp reduction in the surface abundances of lithium and carbon, and reduces the $^{12}\text{C}/^{13}\text{C}$ ratio (see, e.g., Gratton et al. 2000; Lind et al. 2009). As the star evolves along the RGB, there is a further sharp drop in photospheric lithium abundance at the luminosity function bump. Then at the tip of the giant branch, the helium flash causes a rapid and dramatic reconfiguration of the star as it moves to the red clump (RC), establishing a helium-burning core and a much more compact atmosphere. There is not a clear and well-known effect on surface abundances due to the helium flash, though it is reasonable to expect light elements such as lithium to be affected if there is any transport between the surface and the hydrogen-burning shell during this transition.

First dredge-up is a universal event in low-mass stellar evolution, and so we would expect to observe low photospheric lithium abundances in all red giant stars after this stage. However, a small fraction of giant stars, roughly one per cent (Gao et al. 2019), have high photospheric lithium abundances, and some even exceed the primordial lithium abundance (e.g. Yan et al. 2018). Previous studies have uncovered a complex population of lithium-rich giants across a range of evolutionary phases and throughout the Local Group (references include Kraft et al. 1999; Pilachowski et al. 2000; Gonzalez et al. 2009; Kirby et al. 2016). While the first lithium-rich first-ascent red giant branch star was discovered in a globular cluster (Wallerstein & Sneden 1982), only a small number of additional lithium-rich globular cluster stars have been discovered (e.g. Kirby et al. 2016). A fraction of lithium-rich giants exhibit features such as high rotational velocity (e.g., Charbonnel & Balachandran 2000), or infrared excess in their spectral energy distributions (e.g., Rebull et al. 2015), but as a rule they have not been observed to differ in any systematically significant way from lithium-normal giants with the same stellar parameters and evolutionary phase (e.g., Martell & Shetrone 2013; Casey et al. 2016; Smiljanic et al. 2018; Deepak & Reddy 2019).

In response to the observational data, a number of mechanisms have been proposed for the acquisition or production of lithium in evolved stars. These tend to focus on planet engulfment (e.g., Carlberg et al. 2012; Aguilera-Gómez et al. 2016) or internal mixing in conjunction with the Cameron & Fowler (1971) lithium production process (e.g., Charbonnel & Balachandran 2000; Denissenkov 2012). The models are often closely tied to particular events in stellar evolution.

More recent work (e.g., Casey et al. 2019; Singh et al. 2019) has identified that lithium-rich giants are more likely to be in the red clump (i.e., stars that are core-helium burning) than on the first ascent red giant branch (i.e., stars that are hydrogen-shell burning). To evaluate arguments about the source of lithium enrichment it is critical to know the evolutionary phase of the stars in question. It can be difficult to confidently separate red clump stars from red giant

branch stars with similar surface gravity based on photometry or spectroscopy. Asteroseismology has the potential to provide crucial perspective on this problem, as asteroseismic parameters are clearly distinct for RGB stars with degenerate hydrogen cores and RC stars with helium burning cores (Bedding et al. 2011).

With the availability of lithium abundances from large spectroscopic projects like the *Gaia*-ESO Survey (Gilmore et al. 2012), the LAMOST survey (Cui et al. 2012), and the GALAH Survey (Buder et al. 2018), and the tremendous expansion in asteroseismic sky coverage from the *Kepler* (Stello et al. 2013), *K2* (Stello et al. 2017) and *TESS* (Silva Aguirre et al. 2020) missions, we can now assemble and use large catalogues of lithium-rich giants with reliably determined evolutionary states. Recent works (Singh et al. 2019; Gao et al. 2019; Casey et al. 2019; Deepak & Reddy 2019; Deepak et al. 2020) have identified thousands of lithium-rich giants in the Milky Way, a major expansion from the previous small samples.

The goal of this study is to expand the parameter space of the study of lithium-rich giants. The GALAH+ Survey, combining the GALAH, *K2*-HERMES, and *TESS*-HERMES catalogues, provides a large initial set of red giant stars (described in Section 2). From this data set we identify red giant branch and red clump stars using a Bayesian isochrone classification scheme (Section 2.4). We investigate the bulk properties of lithium-rich giant stars, including the distribution in evolutionary phase and the occurrence rate as a function of metallicity (Section 3.1) and other elemental abundances (Section 3.2); we consider observational factors discussed in previous studies including rotational velocity (Section 3.3), binarity (Section 3.5), and infrared excess (Section 3.6); and we explore the kinematic properties of the stars (Section 3.4) to investigate how lithium-rich giants are distributed across Galactic populations. Finally, we discuss our findings and make the case that there are multiple pathways for lithium enrichment in giant stars (Section 4).

2 THE DATA SET

In this section we describe the overall data set (Section 2.1), our giant star selection (Section 2.2), lithium abundance determination (Section 2.3), and classification of stellar evolutionary phase (Section 2.4).

2.1 Observation, reduction, and analysis

Our data set contains 566919 stars, of which the vast majority comes from the merger of the results of the GALAH survey (Martell et al. 2017; Buder et al. 2018), the *K2*-HERMES survey (Wittenmyer et al. 2018; Sharma et al. 2019) and the *TESS*-HERMES survey (Sharma et al. 2018) — the combination of these three surveys is referred to in this work as the GALAH+ survey. All projects that form the GALAH+ survey use the same instrumental setup — the HERMES spectrograph (Sheinis et al. 2015) with the 2dF fibre positioning system (Lewis et al. 2002) at the 3.9-metre Anglo-Australian Telescope — to take high-resolution ($R \sim 28000$) spectra for stars in the Milky Way. HERMES records ~ 1000 Å across four non-contiguous sections of the optical spectrum, including the region around the $H\alpha$ line, which contains the lithium resonance line at 6708 Å.

Each input survey has its own selection function. The main GALAH survey (74 per cent of the GALAH+ data set) uses a simple selection function to acquire a data set from which the underlying properties of the Milky Way can be straightforwardly interpreted: the target catalogue consists of all stars with $12.0 < V < 14.0$,

$\delta < 10$ deg and $|b| > 10$ deg in regions of the sky that have at least 400 targets in π square degrees (the 2dF field of view), and all stars in the same sky region with $9.0 < V < 12.0$ and at least 200 stars per 2dF field of view. The *K2*-HERMES survey (16 per cent of the data set) is aimed at targets from the NASA *K2* mission. This survey typically observes stars in the range $10 < V < 13$ or $13 < V < 14$ with $J - K_S > 0.5$. Most *K2*-HERMES targets observed by *K2* are from the *K2* Galactic Archaeology Program (Stello et al. 2017) which targets stars with $(J - K_S) > 0.5$ (Sharma et al. 2019). The *TESS*-HERMES survey (6 per cent of the data set) was undertaken to improve the scientific outcomes of the *TESS* mission by providing stellar parameters for *TESS* targets more precisely than can be done photometrically (Stassun et al. 2019). Those observations focused on stars in the *TESS* apparent magnitude range ($10.0 < V < 13.1$) in the *TESS* continuous viewing zone within 12 degrees of the Southern ecliptic pole. A further 3 per cent of the data set consists of open and globular cluster targets, and the remaining one per cent is from other targets observed with HERMES that were not part of any of these surveys.

The HERMES data were all reduced with the same custom IRAF pipeline, which is described in Kos et al. (2017), and analysed with the Spectroscopy Made Easy (SME) software (Valenti & Piskunov 1996; Piskunov & Valenti 2017). The analysis is described in detail in Buder et al (in prep), but briefly, SME is used to perform spectrum synthesis for 1D stellar atmosphere models. We use MARCS theoretical 1D hydrostatic models (Gustafsson et al. 2008), with spherically symmetric stellar atmosphere models for $\log g \leq 3.5$ and plane parallel models otherwise. SME calculates radiative transfer under the assumption of local thermodynamic equilibrium, and so we incorporate non-LTE line formation for elements (including lithium, Lind et al. 2009) where the effect on abundance determination is known to be significant. In all cases the non-LTE computations are performed using the same grid of MARCS model atmospheres as the LTE computations.

2.2 Giant star selection

For this work, we are using the GALAH Data Release 3 catalogue of stellar parameters and abundances. At the time of writing this catalog is internal, and it will be publicly released in the second half of 2020¹. This contains 566919 stars with the vast majority also in the *Gaia* DR2 (99.99 per cent of stars; Gaia Collaboration et al. 2016, 2018) and *AllWISE* (96 per cent; Wright et al. 2010; Mainzer et al. 2011) catalogues. This cross-match used the `gaiadr2.allwise_best_neighbour` and `gaiadr2.tmass_best_neighbour` tables created by the *Gaia* mission team.

We apply a number of selections in data quality and stellar parameters to identify a sample of reliable lithium-rich giant stars. We require that each star has:

- the GALAH flag `flag_sp == 0`: no problems noted in the input data, reduction, or analysis;
- the GALAH flag `flag_fe_h == 0`: no problems noted in the iron abundance determination;
- a calculated $E(B - V) < 0.33$ (see Buder et al, in prep);
- a photometric measurement in the *WISE* W_2 band.

We also excluded stars in the SMC or LMC based on their spatial

¹ A link to the public data will be available from <https://galah-survey.org>

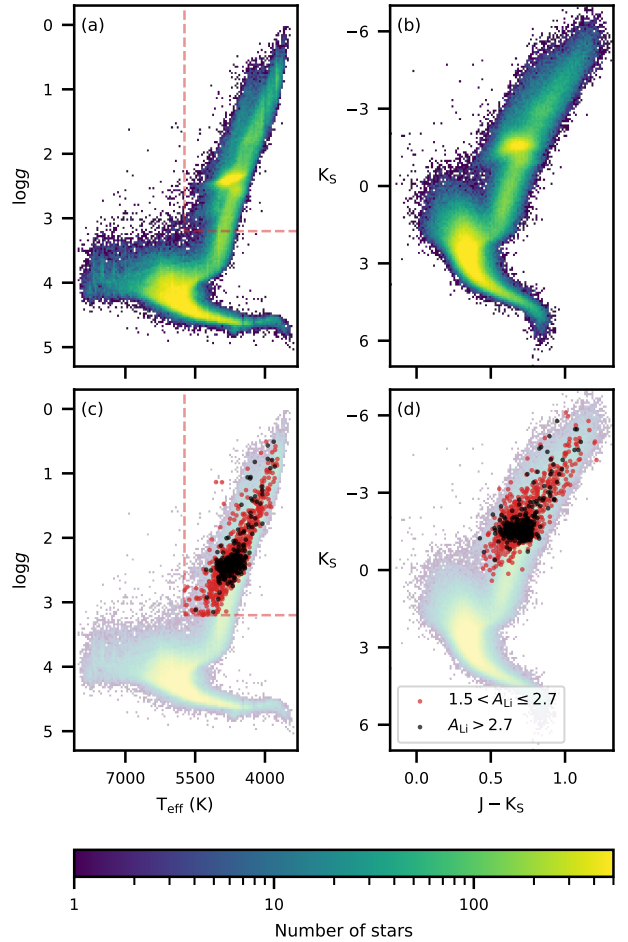


Figure 1. Kiel diagrams (left column) and absolute colour-magnitude diagrams (right column) for the “good” sample (i.e., no flagged problems) of GALAH+ stars considered in this work. The dashed red rectangle in (a) and (c) shows the T_{eff} , $\log g$ selection used to identify giant stars. In the bottom row (c, d) we highlight giant stars with $A_{\text{Li}} > \{1.5, 2.7\}$, using red and black points respectively. This shows that Li-rich giants are found at all parts of the giant branch, but the very Li-enhanced stars ($A_{\text{Li}} > 2.7$) tend to be found in the red clump region.

and kinematic properties². These criteria retained 66.9 per cent (379318/566919) of the sample as “good” stars. Kiel and colour-magnitude diagrams of these stars are shown in Figure 1.

Secondly, we obviously restrict ourselves to giant stars, selecting those stars found to have effective temperature in the range $3000 \text{ K} \leq T_{\text{eff}} \leq 5730 \text{ K}$ and surface gravity in the range $3.2 \geq \log g \geq -1.0$ (red rectangle on Figure 1a,c). Of our sample of “good” stars, 31.6 per cent (120024/379318) were identified as giant stars.

² The LMC selection includes all stars within 5 deg of (RA, Dec) = (78.00, -68.08) deg, with a proper motion within 1.5 mas yr^{-1} of $\mu_{\text{RA}}, \mu_{\text{Dec}} = (1.80, 0.25)$ and a radial velocity larger than 215 km s^{-1} . The SMC selection includes all stars within 5 deg of (RA, Dec) = (11.83, -74.11) deg, with a proper motion within 1.5 mas yr^{-1} of $\mu_{\text{RA}}, \mu_{\text{Dec}} = (0.85, -1.20)$, a radial velocity larger than 80 km s^{-1} , and a parallax $\varpi < 0.08 \text{ mas}$.

2.3 Lithium abundances

The lithium abundance of each star was determined as part of the main analysis of the GALAH+ data set from synthesis of the 6708 Å lithium line. We report the lithium abundance value in the form of $A_{\text{Li}}(\equiv [\text{Li}/\text{Fe}] + [\text{Fe}/\text{H}] + 1.05)$, where the A_X abundance scale gives the number density of element X on a logarithmic scale relative to hydrogen, $A_{\text{H}} = 12$ by definition, and 1.05 is the lithium abundance of the Sun (Asplund et al. 2009). We follow the typical convention from the literature of considering a giant star to be lithium-rich if its abundance $A_{\text{Li}} > 1.5$ (see the discussion in Kirby et al. 2016, on whether this Li-rich limit should be a function of stellar parameters). We also highlight throughout this work the subset of these Li-rich giant stars with A_{Li} above the primordial value of 2.7 (Cyburt et al. 2008; Fields et al. 2020), because it serves as a useful landmark in the abundance space.

Each elemental abundance in GALAH+ has an associated reliability flag. For this work we require `flag_li_fe == 0`, which indicates a significant line detection with no flagged problems. Of the 120024 “good” giant stars, 10828 stars (9.0 per cent) met this criterion. As with any spectral line, the strength of the lithium line is a complicated function of the stellar parameters and the lithium abundance of the star. In Figure 2 we show example HERMES spectra for giant stars of similar $[\text{Fe}/\text{H}]$ across the range of T_{eff} and $\log g$ values covering the giant branch. Each panel shows the spectrum of one Li-rich giant (red line; in all cases $A_{\text{Li}} \sim 2.3$), compared to the spectra of 10 randomly selected stars with similar stellar parameters (grey lines). This highlights that for most giant stars, the 6708 Å line of lithium is not detectable, and that the sensitivity to lithium abundance decreases as T_{eff} rises. This explains why only 9 per cent of our giant star sample has a measured (and non-flagged) value for A_{Li} , despite our high quality spectra.

Very high lithium abundances are also challenging for our abundance pipeline to determine correctly, since at high abundance the curve of growth becomes flatter and consequently small changes in line strength would require larger changes in abundance. For this reason, in GALAH+ DR3 we have flagged all lithium abundances above $A_{\text{Li}} \sim 4.6$ as unreliable. There may be a number of very lithium-rich stars in the data set that do not have abundance values in our current catalogue. These stars will require boutique analysis for accurate abundance determination.

For our giant star sample, 1306/120024 (1.1 per cent) have $A_{\text{Li}} > 1.5$. This is consistent with the 1.29 per cent value found independently in the LAMOST survey (Gao et al. 2019). Of our 1306 Li-rich giants, 329 stars lie above the primordial value of $A_{\text{Li}} = 2.7$ — we refer to these stars throughout as “super Li-rich”.

The location of our Li-rich giants in the Kiel and color-magnitude diagrams are shown with red and black points on Figure 1. On the lower giant branch ($\log g \sim 3$), there is a dearth of Li-rich stars on the cooler side of the giant branch. This has been previously observed (Ramírez et al. 2012; Buder et al. 2018), and is caused by the deeper surface convective envelopes of cooler stars, which extend to hotter regions in the stellar interior and allow for more depletion of the surface lithium abundance.

2.4 Classifying evolutionary phase

The evolutionary state of lithium-rich giants is an essential piece of knowledge for evaluating models to explain their enrichment. The GALAH+ survey observes two main populations of low-mass giants in the Milky Way:

- Red giant branch (RGB) stars, on their first ascent of the giant

branch, with an inert helium core and a hydrogen-burning shell. The RGB spans a wide range in $\log g$ and luminosity.

- Red clump (RC) stars, in the stage directly after the first ascent of the giant branch, with a helium-burning core and a hydrogen-burning shell. RC stars occupy only a small range of He core mass and therefore luminosity, and they fall near RGB stars with the same $\log g$ in the observable parameter space.

About one-third of evolved stars in a magnitude-limited survey are expected to be RC stars (Girardi 2016). As noted by previous authors (Casey et al. 2019; Gao et al. 2019; Zhang et al. 2020), Li-rich giants are more likely to be RC stars than RGB. As shown in the bottom row of Figure 1, there is a clear over-density of stars corresponding to the location of the red clump, both for the Li-rich and super-Li-rich stars.

As discussed in Section 1, RC and RGB stars can be distinguished using asteroseismology. Our ability to infer the interior properties of stars has been greatly improved by the precise photometry recorded by various space missions (e.g., *CoRoT*, *Kepler*, *K2*, *TESS*). The gravity-mode period spacing ($\Delta\Pi$), the frequency offset (ϵ), and the large frequency spacing ($\Delta\nu$) can be measured from the power spectra derived from these light curves, and these quantities take very different distributions for red clump and red giant branch stars (e.g., Mosser et al. 2012; Kallinger et al. 2012; Stello et al. 2013; Vrad et al. 2016). This technique has been used for small samples of Li-rich giants to get unambiguous classifications (Singh et al. 2019; Casey et al. 2019), and the asteroseismic quantities can be used to train data-driven methods for spectroscopic classification (e.g., Hawkins et al. 2018).

Most of our giant stars do not have the necessary time-series photometry for asteroseismic determination of their evolutionary phase. The time series photometry in *K2* and *TESS* is not as extensive as it was for the original *Kepler* mission, making measurements of the seismic properties more difficult to obtain, especially for $\Delta\Pi$. However, classification of red clump versus red giant branch stars can be done reliably from *K2* data using well-trained machine learning methods. For this work, we used classifications performed using the method described in Hon et al. (2018), which has a 95 per cent accuracy. 990 of the *K2* stars in our sample have reliable stellar parameters and seismic classifications from this technique. Of these, 568 stars are classified as RC and 422 are RGB, but only 8 of the 990 stars are lithium-rich. We indicate these stars throughout this work, but do not rely on them for any of the conclusions.

Since only a small fraction of our Li-rich giants have seismic classifications, for the majority of our stars we used RGB/RC classifications from the Bayesian Stellar Parameters estimator (bSTEP). This is described in detail in Sharma et al. (2018), but briefly, it provides a Bayesian estimate of intrinsic stellar parameters from observed parameters by making use of stellar isochrones. For results presented in this paper, we exploit the PARSEC-COLIBRI stellar isochrones (Marigo et al. 2017). The red-clump evolutionary state is labelled in the isochrones and we make use of this information to assign a Bayesian probability for a star belonging to the red clump based on its observed stellar parameters. We supplement these classifications by taking advantage of the fact that RC stars are standard candles. The *WISE* W_2 absolute magnitude of the stars was calculated using the conventional relationship $M_\lambda = m_\lambda - 5 \log(r_{\text{est}}) + 5$, with the distance r_{est} taken from Bailer-Jones et al. (2018). The vast bulk of our RC stars were found in the range $W_2 = -1.63 \pm 0.80$, in line with expectations (Karaali et al. 2019; Plevne et al. 2020). Our RC and RGB selections are made as follows:

Table 1. We identify 1306 Li-rich giants with reliable evolutionary stage classifications. Here we give their *Gaia* DR2 `source_id`, sky locations, and GALAH+ stellar parameters and spectroscopic information. The full version of the table is available online; the first six entries included here are the Li-rich stars shown in Figure 2, and the seventh entry is the star with the highest A_{Li} in our sample.

source_id	RA	Dec	RV (km s ⁻¹)	T_{eff} (K)	log g	[Fe/H]	A_{Li}	RC or RGB
6137526858900209920	199.020	-41.767	-24.42 ± 0.29	3970 ± 72	1.63 ± 0.22	-0.17 ± 0.05	2.25 ± 0.06	RGB
5371899834025124608	175.501	-48.171	1.43 ± 0.66	4285 ± 158	1.75 ± 0.26	-0.22 ± 0.17	2.21 ± 0.23	RGB
6100901881763791232	223.933	-42.034	-18.00 ± 0.33	4429 ± 80	2.01 ± 1.20	-0.18 ± 0.05	2.40 ± 0.08	RGB
6235140814020759808	236.883	-25.259	-23.43 ± 0.55	4681 ± 127	2.31 ± 0.26	-0.18 ± 0.11	2.25 ± 0.16	RC
6129493448995721984	180.111	-50.437	-50.04 ± 0.33	4980 ± 80	2.55 ± 0.21	-0.21 ± 0.05	2.25 ± 0.08	RC
3155263089390175872	109.992	9.198	38.66 ± 0.58	5147 ± 127	2.72 ± 0.24	-0.18 ± 0.11	2.29 ± 0.16	RC
6142572036722901504	197.384	-37.155	31.26 ± 0.29	4218 ± 73	0.82 ± 0.34	-1.31 ± 0.05	4.54 ± 0.06	RGB

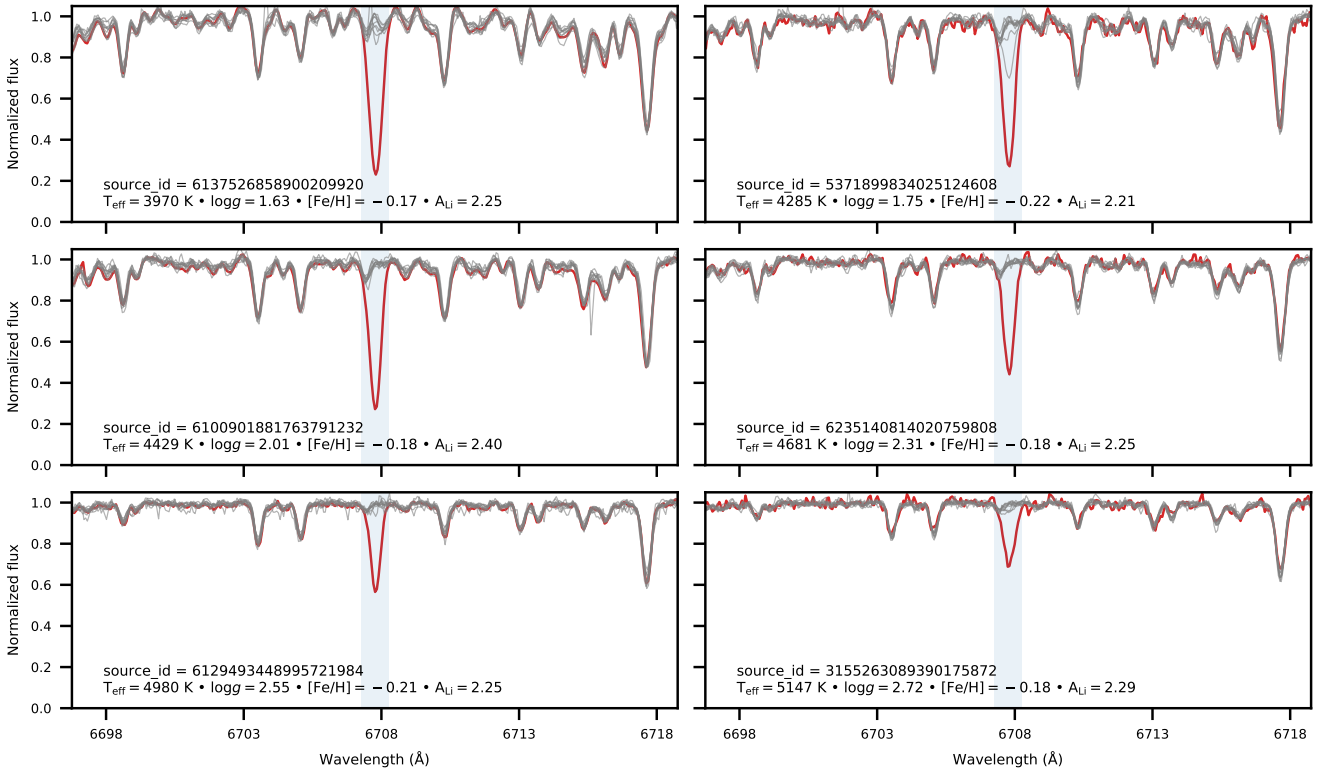


Figure 2. Examples of the spectral region containing the Li 6708 Å line (indicated with the shaded blue region in each panel), as observed with HERMES, for stars from a range of T_{eff} and log g along the giant branch. In each panel we highlight one Li-rich giant star (red line; also the `source_id` and stellar parameters) and 10 other randomly selected stars with similar stellar parameters (grey lines) — namely $\Delta(T_{\text{eff}}) < 50$ K, $\Delta(\log g) < 0.2$, $\Delta([\text{Fe}/\text{H}]) < 0.03$, $\Delta([\alpha/\text{Fe}]) < 0.05$, $v_{\text{broad}} < 5$ km s⁻¹. In all panels, the Li-rich stars have approximately the same metallicity and A_{Li} . There are two things to note: first, for most of these giant stars, the lithium line is either weak or not visible; second, for a given A_{Li} , the lithium absorption line gets weaker with increasing T_{eff} — which means that the minimum detectable A_{Li} in our data set is higher at higher temperature.

- RC stars: $\text{BSTEP RC probability} \geq 0.5$ and absolute magnitude $|W_2 + 1.63| \leq 0.80$,
- RGB stars: $\text{BSTEP RC probability} < 0.5$ or absolute magnitude outside the range $|W_2 + 1.63| > 0.80$.

In Table 2 we compare the results from the seismic and isochrone-based **BSTEP** classifications. Considering, for instance, the red clump stars, the **BSTEP** classification recalls 90 per cent (510/568) of red clump stars identified from asteroseismology. For the RGB stars this recall rate is 66 per cent. Conversely, of the 654 stars classified as RC stars by **BSTEP**, only 510 were classified as RC

by the seismic method, giving a precision of 78 per cent. Similarly, for the RGB stars the precision is 83 per cent.

Using the **BSTEP** classification of RC and RGB stars for our full set of 120024 giants, 44767 (37.3 per cent) are on the RC, and 75257 (62.7 per cent) belong to the RGB — as expected for a magnitude-limited survey (Girardi 2016). These results are presented in Figure 3 and in Table 3. The expected morphologies in the Kiel and absolute colour-magnitude diagrams are recovered; namely, in the Kiel diagram, the RC can be divided into the primary red clump and the secondary red clump that consists of slightly more massive stars,

Table 2. Comparison of the classifications of the RC and RGB stars for those stars that have classifications from both [Hon et al. \(2018\)](#) and our `BSTEP` selection, with recall and precision rates included. As an example, 568 stars were classified as RC stars using their seismic information and 510 of these 568 were classified as RC stars using `BSTEP`: a 90 per cent recall rate. Conversely, 654 stars were classified as RC by `BSTEP`, and the same 510 of these were classified as RC from seismic information: 78 per cent precision rate.

	RC (seismic)	RGB (seismic)	Total
RC (<code>BSTEP</code>)	510 (90%; 78%)	144	654
RGB (<code>BSTEP</code>)	58	278 (66%; 83%)	336
Total	568	422	990

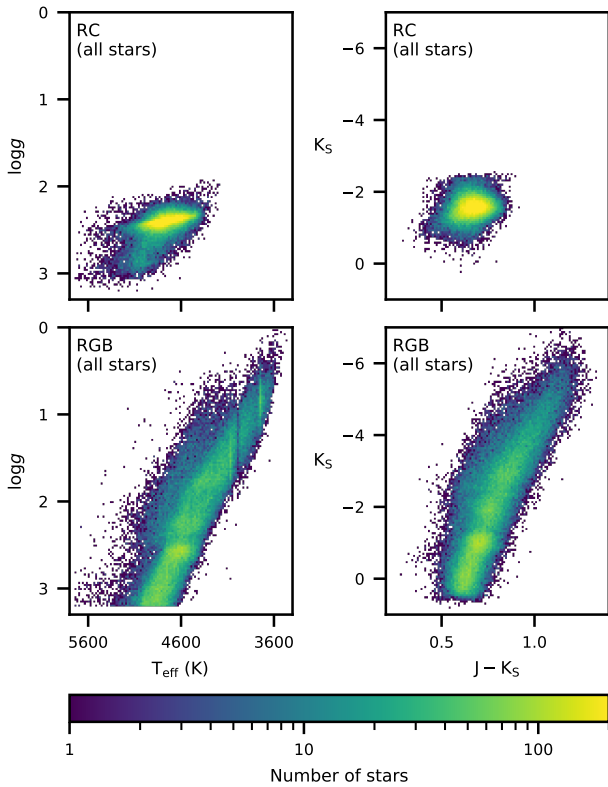


Figure 3. Kiel diagrams (left column; T_{eff} vs $\log g$) and absolute colour-magnitude diagrams (right column) for the stars selected to be from (top row) RC, and (bottom row) RGB. For the RC stars both the primary RC and the higher $\log g$ secondary RC can be seen. In the RGB panels the region of higher density on the lower giant branch is the RGB bump.

and the RGB shows evidence for the luminosity function bump at a slightly higher $\log g$ than the bulk of the RC.

One of the essential observables for Li-rich giants is the distribution in evolutionary phase, since different models for Li enrichment may be tied to particular processes — for example, planet engulfment should happen during the RGB phase, while the star is expanding dramatically, but not afterward. It is important to consider this distribution not just in the sheer number of stars at a particular evolutionary phase, but rather in terms of the probability for a star at a given phase to be Li-rich. However, this statistic has

Table 3. Counts of RGB and RC stars from our `BSTEP` classification, and the number of stars that are Li-rich ($A_{\text{Li}} > 1.5$) and super Li-rich ($A_{\text{Li}} > 2.7$). Using the mass estimates from `BSTEP`, stars below 1.7 solar masses are classed as primary RC (pRC) stars, and stars above this mass as secondary RC (sRC) stars. The first percentage shows the proportion with respect to that of the total population of that type — e.g., for Li-rich RC stars, $888/1306 = 68$ per cent. For columns with a second percentage, this shows the percentage of the previous column value, e.g., there are 75 super Li-rich RGB stars, which is 18 per cent of the total number of Li-rich RGB stars (418).

Star type	Total stars	Li-rich	Super Li-rich
All giants	120024	1306 (1.1%)	329 (25.2%)
RGB	75257 (63%)	418 (32%; 0.6%)	75 (23%; 18%)
RC	44767 (37%)	888 (68%; 2.0%)	254 (77%; 29%)
pRC	41304 (34%)	763 (58%; 1.8%)	244 (74%; 32%)
sRC	3463 (2.9%)	125 (9.6%; 3.6%)	10 (3.0%; 8.0%)

not been reported previously. We find that $p(\text{Li}|\text{RC})$, the probability for an RC star to be Li-rich, is 2.0 per cent ($888/44767$). This is three times $p(\text{Li}|\text{RGB})$, the probability for an RGB star to be Li-rich ($418/75257$; 0.6 per cent). This implies complexity in the process of Li enrichment, perhaps indicating that it occurs in a larger fraction of RC stars than RGB stars, or that there is a longer timescale for re-depletion of Li from the atmosphere in RC stars, or that there are other factors at work. Assembling a thorough sample of the intrinsic and observable properties of Li-rich and Li-normal giants is crucial for constraining and improving models for Li enrichment.

3 LITHIUM-RICH GIANTS AS A STELLAR POPULATION

In this section we compare and contrast Li-normal and Li-rich giants in the fundamental stellar parameters T_{eff} , $\log g$ and $[\text{Fe}/\text{H}]$ (Section 3.1), elemental abundances (Section 3.2), rotation rates (Section 3.3), stellar kinematics (Section 3.4), binarity (Section 3.5), and infrared excess (Section 3.6).

3.1 Lithium-rich giants across the stellar parameter space

Figure 4 presents A_{Li} for our giants with respect to their basic stellar parameters: T_{eff} , $\log g$, $[\text{Fe}/\text{H}]$. The upper row shows only red clump stars, and the lower row shows only red giant branch stars. The same stars are shown in all three columns, and stars with asteroseismic classifications are represented with star shapes. Horizontal lines mark the typical definition of "lithium-rich" at $A_{\text{Li}} = 1.5$ and the primordial lithium abundance, $A_{\text{Li}} = 2.7$.

There is a T_{eff} -dependent lower envelope to the lithium abundance that can be measured for giant stars in GALAH+, which is a result of a weaker 6708 Å resonance line at higher T_{eff} , for a fixed A_{Li} — see the spectra plotted in Figure 2 and the discussion in Section 2.3. It is possible that we have failed to measure abundances for some of the hotter Li-rich giants.

As shown in Figure 3, the red clump stars observed by GALAH+ can be split into two main populations: the lower mass primary RC (pRC) and the higher mass secondary RC (sRC). In Figure 4 they are most readily distinguished in the top-middle panel, where to aid the reader, there is a vertical line at $\log g = 2.7$ that roughly separates the sRC from the pRC. Of particular note is that only a handful of stars on the sRC are super Li-enriched ($A_{\text{Li}} > 2.7$). Using the mass estimated for each star by `BSTEP`, the RC sample can

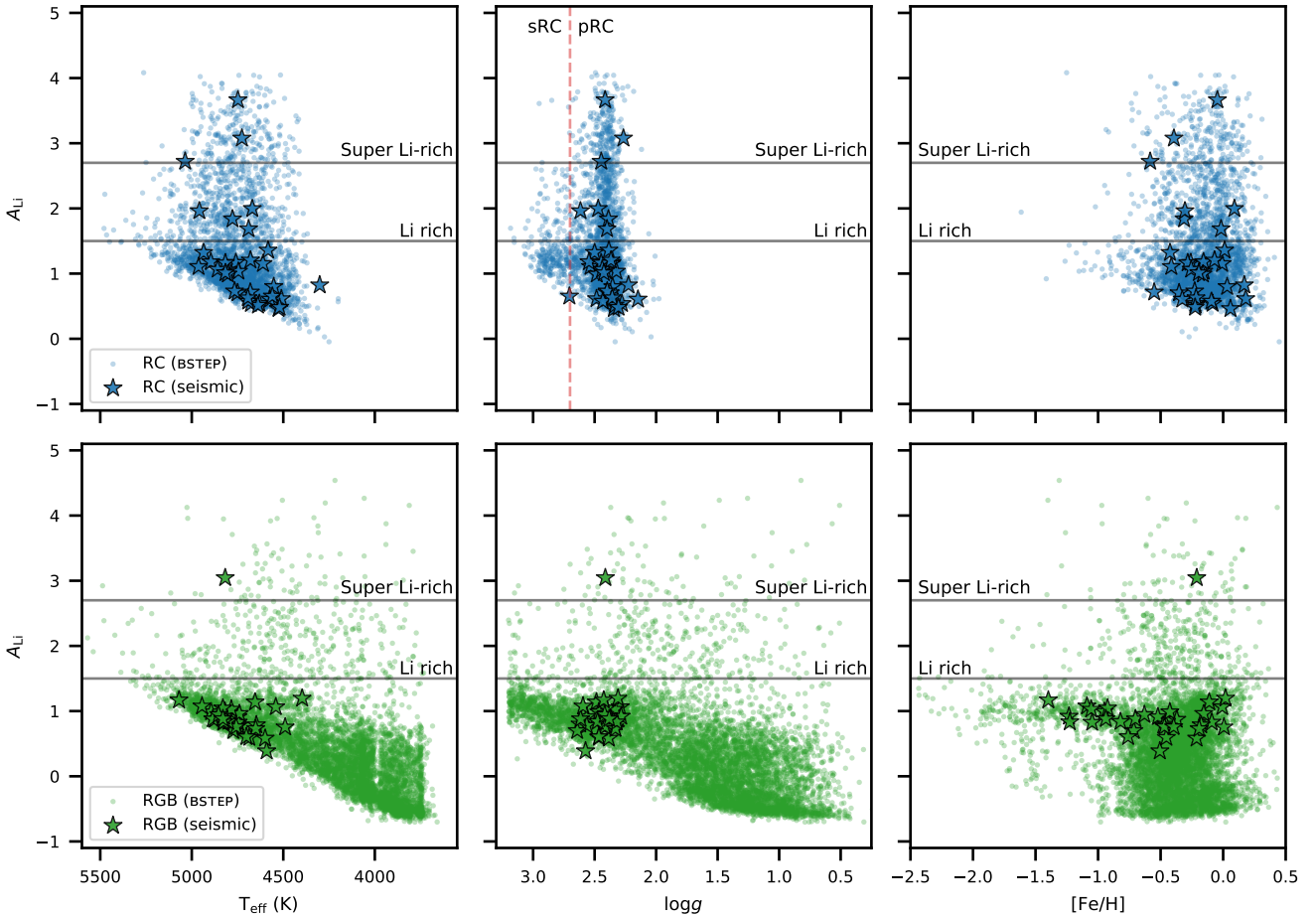


Figure 4. Comparing the A_{Li} abundances with respect to T_{eff} (left column), $\log g$ (middle column), and $[\text{Fe}/\text{H}]$ (right column). These are split into the red clump sample (upper panel of each column) and red giant branch sample (lower panel of each column). In all panels we show the stars classified as RC or RGB by the isochrone-based `bSTEP` method (dots) and the asteroseismic classifications (black-edged star symbols). The horizontal lines in all panels indicate criteria for whether a star is Li-rich or super Li-rich. In the T_{eff} panels there is a clear lower envelope in A_{Li} , indicating a detection limit driven by line strength. In the $\log g$ panel for RC stars (upper middle) we highlight the regions occupied by the secondary red clump (sRC) and primary red clump (pRC) to note the lack of super Li-rich sRC stars. In the $[\text{Fe}/\text{H}]$ RC panel there is a distinct lack of Li-rich stars with $[\text{Fe}/\text{H}] < -1$, which is real and not a matter of sensitivity to lithium line strength.

be divided into pRC stars ($M_* < 1.7$ solar masses; Girardi 2016) and sRC stars ($M_* \geq 1.7$ solar masses). There are 3463 sRC stars, of which 125 are Li-rich, but only 10 of these are super Li-rich — 0.3 per cent of sRC stars and 8.0 per cent of Li-rich sRC stars. Meanwhile, there are 41304 pRC stars, of which 763 are Li-rich, and 244 are super Li-rich (0.6 per cent; 31.9 per cent). This indicates that the mass of an RC star is an important part of whether it can become Li-rich, with a higher likelihood for low-mass RC stars.

The luminosity function bump may play an important role in the study of Li-rich giants. As an event characterised by the introduction of fresh fuel into the hydrogen burning shell and an opportunity for increased mixing between the surface and the interior, it may be responsible for both further lithium depletion (e.g., Lind et al. 2009) and Cameron-Fowler lithium production (e.g., Charbonnel & Balachandran 2000), depending on the exact conditions. There does appear to be a dearth of Li-rich RGB stars at the high-gravity end of the RGB star distribution. However, this picture is complicated, as stars below the RGB bump will also be hotter and therefore closer to the lithium detectability limit.

The right column of Figure 4 shows the behaviour of A_{Li} with metallicity for our giant stars, separated into the RC and RGB populations. The RC cohort clearly lacks stars with $[\text{Fe}/\text{H}] < -1$, which is to be expected for red clump stars in the Milky Way — there is a minimum mass for RC stars, and as a result they are a moderately young and metal-rich population (e.g., Ramírez et al. 2012). The evolution of metal-poor RC stars is also faster than for more metal-rich RC stars (Girardi 2016), making them less likely to be observed.

The metal-poor RGB stars are almost exclusively below the Li-rich threshold, with a concentration at $A_{\text{Li}} \approx 1.0$. These stars are mainly located near the luminosity function bump, indicating that first dredge-up has reduced their A_{Li} abundance to around 1, and it will continue to fall as they evolve along the RGB as a consequence of deep mixing (e.g., Lind et al. 2009; Angelou et al. 2015).

There has been some tension in the literature between the < 1 per cent occurrence rates of Li-rich giants in the low metallicity environments of globular clusters (see e.g., Kirby et al. 2012), and the > 1 per cent rate observed in the disk of the Milky Way.

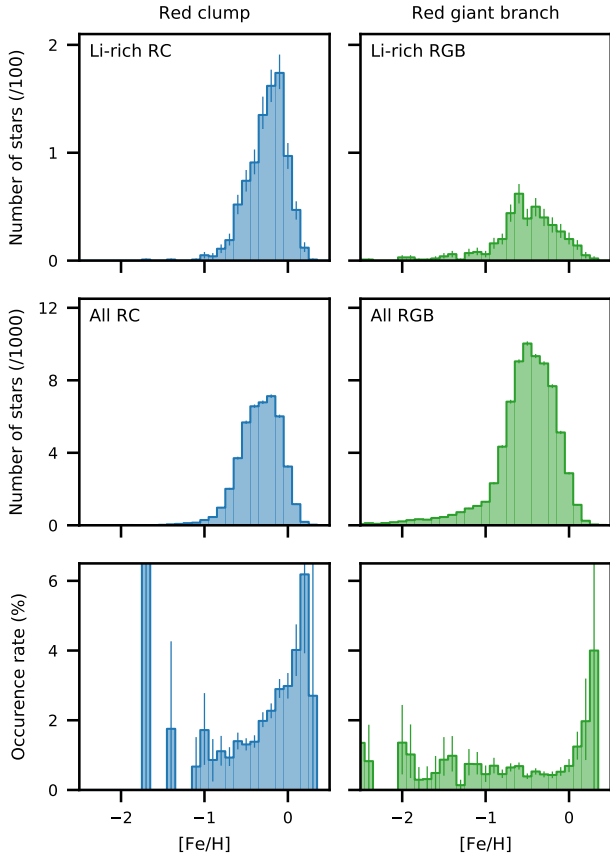


Figure 5. Comparing the occurrence rate of Li-rich giants with changing $[\text{Fe}/\text{H}]$ in the RC (left column) and RGB (right column) cohorts (here just showing the `BSTEP` classification method results). In the top panel of each column is the $[\text{Fe}/\text{H}]$ distribution of Li-rich giants from each cohort; the middle panel is the $[\text{Fe}/\text{H}]$ distribution of all stars in each cohort (whether or not they have a measured A_{Li}); and the bottom panel of each column is the occurrence rate with $[\text{Fe}/\text{H}]$ (i.e. the top panel ‘divided’ by the middle panel). The uncertainty of each bin in the histogram was calculated from 1000 bootstrap samples of the iron abundance values. The occurrence rate of Li-rich giants in both groups rises at high metallicity, but the distributions are quite different — for the RC stars there is a steady increase of occurrence rate with metallicity, while for RGB stars, the occurrence rate is relatively flat below $[\text{Fe}/\text{H}] = 0$.

Recent works with larger data sets (e.g., Casey et al. 2019; Deepak et al. 2020) have quantified this as a more general increase in the occurrence rate of lithium-rich giants with increasing metallicity. In Figure 5 we consider the occurrence rate of Li-rich giants with metallicity in our RC and RGB cohorts independently. The uncertainty of each bin in the histogram was calculated from 1000 bootstrap samples of the iron abundance values. The metallicity distribution of the Li-rich giants is qualitatively similar to the distribution for all giants. As would be expected for the GALAH+ sample, which is comprised mainly of Galactic disc stars, the distribution peaks near solar metallicity. For the RGB sample there is a tail of stars to low metallicity.

The occurrence rate of Li-rich giants in both groups rises at high metallicity, but the distributions are quite different. For the RC stars there is a steady increase of occurrence rate with metallicity, while for RGB stars, the occurrence rate is relatively flat from

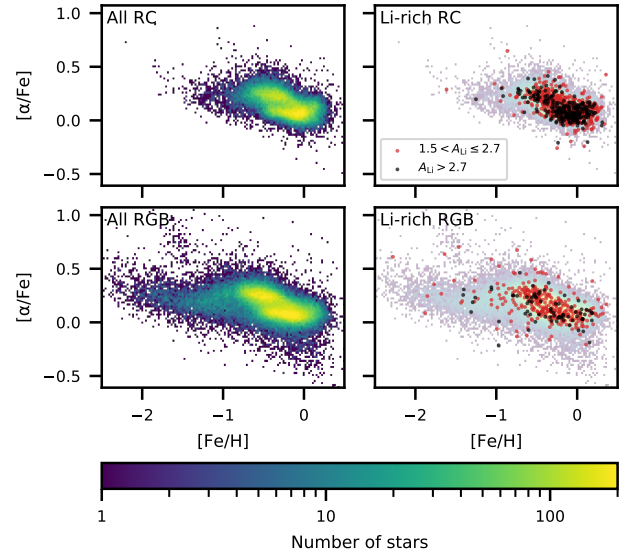


Figure 6. Comparison of the $[\alpha/\text{Fe}]$ abundances of the RC (top row) and RGB (bottom row) stars. In the right column we further highlight the Li-rich (red dots) and super Li-rich (black dots) giants. The majority of super Li-rich RC stars belong to the α -poor ‘thin disc’ population.

$-2 < [\text{Fe}/\text{H}] < 0$, and then increases dramatically for stars with super-solar metallicity (though with larger error bars due to the smaller number of stars observed at these metallicities). We interpret this increase as a sign of multiple lithium enrichment processes at work, with the dominant mechanism for red clump stars being quite sensitive to stellar metallicity, the dominant process for RGB stars with sub-solar metallicity being independent of metallicity, and potentially a third lithium enrichment process for metal-rich RGB stars.

3.2 Other elemental abundances in Li-rich giants

The abundances of other elements in Li-rich giants could provide information about the processes by which the lithium abundance of some giants is enhanced. GALAH+, which provides abundances for a wide range of elements from a variety of nucleosynthetic pathways, gives a great opportunity to explore this.

Interestingly, there are only a few elements in GALAH+ DR3 that show any obvious differences between the abundance patterns of Li-normal and Li-rich giants. In this section we discuss $[\alpha/\text{Fe}]$ (Section 3.2.1) and $[\text{C}/\text{Fe}]$ (Section 3.2.2), as this was recently highlighted by Deepak et al. (2020) as showing possible correlations with lithium enrichment.

3.2.1 Alpha elements

For GALAH+ DR3, $[\alpha/\text{Fe}]$ is the error-weighted combination of the abundances determined from selected Mg, Si, Ca, and Ti lines. Figure 6 shows that Li-rich (red dots) or super Li-rich (black dots) RC stars appear to be preferentially located at low $[\alpha/\text{Fe}]$ values and high $[\text{Fe}/\text{H}]$.

To explore this further, we can compare $p(\text{Li-rich}|\alpha\text{-high,RC})$, the probability that an α -high RC star is Li-rich, against $p(\text{Li-rich}|\alpha\text{-low,RC})$, the probability that an α -low RC star is Li-rich. We find that α -low RC stars are somewhat more likely to be

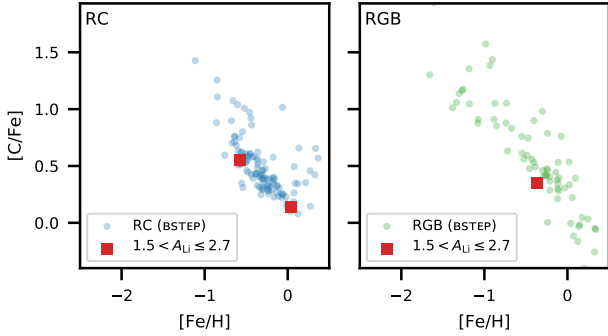


Figure 7. Carbon abundance $[C/Fe]$ for the RC (left) and RGB (right) stars. Carbon can only be measured in HERMES spectra for a small minority of giant stars where it is abundant. The carbon abundance of Li-rich giants is of interest because the two elements are depleted together during first dredge-up, and carbon may also be destroyed by fusion processes at temperatures that can destroy lithium. Only three of the Li-rich giants (all with $1.5 < A_{Li} \leq 2.7$) have a measured $[C/Fe]$, and they follow the A_{Li} behaviour of the other stars with measured $[C/Fe]$.

Li-rich than α -high RC stars: $p(\text{Li-rich}|\alpha\text{-high,RC}) = 0.015$ (278/19165), while $p(\text{Li-rich}|\alpha\text{-low,RC}) = 0.024$ (610/25602). For super Li-rich stars, the probabilities are $p(\text{Li-super}|\alpha\text{-high,RC}) = 0.004$ (74/19091), while $p(\text{Li-super}|\alpha\text{-low,RC}) = 0.007$ (180/25602). Hence the α -low population is nearly twice as likely to be Li-rich (1.6 times) or super Li-rich (1.75 times) as compared to the α -high population.

The apparent affinity between high A_{Li} and low $[\alpha/Fe]$ does not happen because the lithium enrichment process destroys α elements, or is hampered by their presence. Rather, it is related to the properties of the Galactic components that are captured in our observational sample, similar to the effect seen by Ramírez et al. (2012). For stars in the Milky Way disc, including the majority of our RC stars, $[\alpha/Fe]$ is anticorrelated with metallicity. As shown in Figure 5, the occurrence rate of Li-rich RC stars increases with metallicity, with the result that there are more Li-rich stars in the α -low population.

In contrast to RC stars, RGB stars in both the Li-normal and Li-rich subsets extend to lower $[Fe/H]$ and higher $[\alpha/Fe]$, and the distributions of the Li-normal and Li-rich RGB stars in Figure 6 look quite similar to each other, with perhaps an excess of Li-rich stars at $[Fe/H] > 0$. This is consistent with the occurrence rate of Li-rich RGB stars shown in Figure 5, which is flat for $[Fe/H] < 0$ but rises thereafter. RGB stars have higher luminosities than RC stars, and as a consequence in a magnitude limited survey like ours they are drawn from a larger volume including more of the thick disk and the halo. This, in addition to the dependence of occurrence rate on metallicity, skews the distribution of Li-rich RC stars toward low $[\alpha/Fe]$ and high metallicity relative to RGB stars.

3.2.2 Carbon

Deepak et al. (2020) recently explored the other elemental abundances of Li-rich and Li-normal giants using the GALAH DR2 data set. They found that for all the elements available, the only element that showed an appreciable difference between the two populations was carbon. Unfortunately, this result relied upon abundances that had been identified by the GALAH team as unreliable (i.e., the quality flags on the abundances were non-zero). Figure 7 shows the non-flagged (i.e., reliable) carbon abundances for RC and RGB stars

Table 4. Comparison of how many RC and RGB stars are rapid rotators. Rapid rotators are defined as those stars with detrended $v_{\text{broad}} > 10 \text{ km s}^{-1}$. In the last column, the first percentage is the proportion of all stars of that class that are Li-rich rapid rotators, and the second percentage is the proportion of rapid rotators of that class. RC stars are about twice as likely as RGB stars to be rapid rotators (4.1 per cent versus 2.4 per cent), but the proportion of Li-rich stars that are rapid rotators is higher for RGB stars than RC stars (19 per cent versus 13 per cent).

	Total stars	Rapid rotators	Li-rich rapid rotators
All giants	120024	3656 (3.0%)	165 (0.14%; 13%)
RC	44767	1830 (4.1%)	87 (0.19%; 9.8%)
RGB	75257	1826 (2.4%)	78 (0.10%; 19%)

in GALAH+ DR3. The spectroscopic features of carbon captured in HERMES spectra are quite weak in the bulk of giant stars, and therefore our sensitivity to $[C/Fe]$ is limited. This produces a clear detectability trend that can be seen in the Figure, where lower $[C/Fe]$ abundances are only detected for more metal-rich stars. Only three of the Li-rich giants (all with $1.5 < A_{Li} \leq 2.7$) have a measured $[C/Fe]$, and they follow the A_{Li} behaviour of the other stars with measured $[C/Fe]$.

Interestingly, we do derive reliable (and high) carbon abundances for a number of stars. First dredge-up and subsequent mixing processes typically result in sub-solar $[C/Fe]$ for giant stars (e.g., Lagarde et al. 2019). Carbon-richness at this stage in stellar evolution often indicates mass transfer from an asymptotic giant branch (AGB) companion, and may be accompanied by other chemical tags of AGB nucleosynthesis including s-process elements (e.g., Hansen et al. 2016; Karakas & Lugaro 2016). The topic of carbon-enhanced giant stars in GALAH+ DR3 is outside the scope of this paper, but bears further investigation.

3.3 Stellar rotation

The rotation rates of Li-rich giants are of interest because one of the proposed modes of lithium enhancement is rotationally induced mixing, which can raise the surface lithium abundance via the process described by Cameron & Fowler (1971).

As part of the spectroscopic analysis in GALAH+, an overall spectral broadening parameter v_{broad} is calculated, which encompasses macroturbulence and rotational velocity. Typically in RGB stars, the macroturbulence velocity is on the order of 7 km s^{-1} (Carney et al. 2008b). We can therefore interpret stars with v_{broad} distinctly above 7 km s^{-1} as having a significant rotational velocity component.

In Figure 8 we show the distributions of v_{broad} with $\log g$ for RC and RGB stars separately. As expected, v_{broad} increases in stars as they ascend the giant branch (e.g., Carney et al. 2008a). We can see that most stars are found with $5 < v_{\text{broad}} < 10 \text{ km s}^{-1}$, so most stars in our sample do not have appreciable rotational velocity. In order to identify stars with v_{broad} that differs markedly from the average for their $\log g$, we fitted the overall trend in v_{broad} as a function of $\log g$ by dividing the stars into 100 bins in $\log g$ in the range $0.5 < \log g < 3.2$. In each bin we found the median v_{broad} value and then fit an exponential function of the form $v_{\text{broad}} = a \exp(-b \times \log g) + c$. This fit is shown as the left red dashed curve on all panels of Figure 8. This was then used to ‘detrend’ the v_{broad} with respect to $\log g$, so that detrended $v_{\text{broad}} = v_{\text{broad}} - [a \exp(-b \times \log g) + c]$.

We interpret stars with detrended v_{broad} larger than 10 km s^{-1}

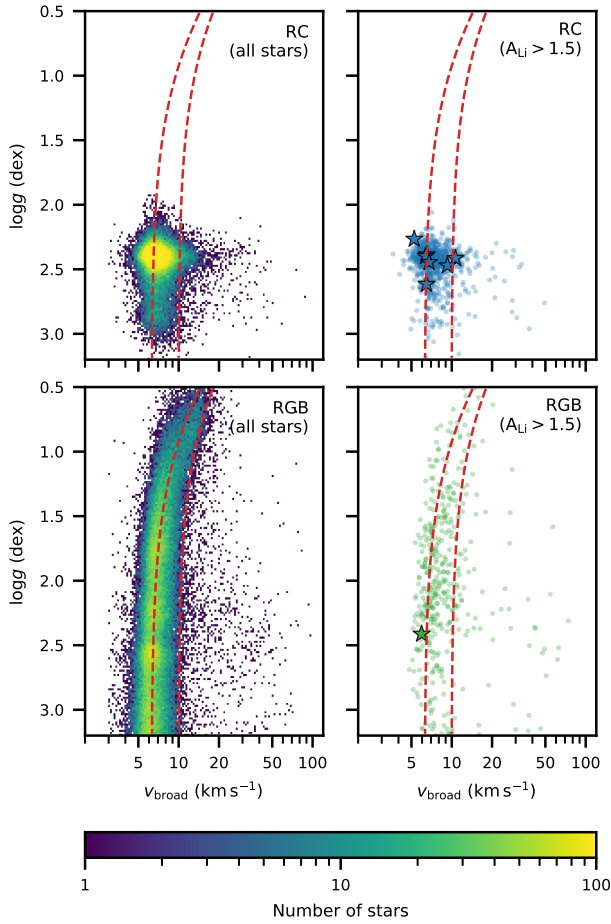


Figure 8. The v_{broad} distributions of the red clump (top row) and red giant branch (bottom row) samples. The quantity v_{broad} is a broadening term measured from the stellar spectra that encompasses macroturbulence and rotational velocity. The left column shows all giants from the RC and RGB cohorts, while the right column shows just the Li-rich stars ($A_{\text{Li}} > 1.5$). As in Figure 4, in the right column we highlight the stars identified seismically as RC or RGB with star shapes. On all panels, the left red curve shows the fitted relationship between v_{broad} and $\log g$ for all giant stars. The right dashed curve is offset by $+3.68 \text{ km s}^{-1}$, corresponding to a detrended v_{broad} of 10 km s^{-1} for the faintest RGB stars in our sample. We interpret stars to the right of the right curve as being rapid rotators. Notably, Li-rich RGB stars are more likely to be rapid rotators than Li-rich RC stars.

as “rapid rotators”. In Table 4 we list the number of stars above this threshold. With this rapid rotation definition, 3.0 per cent (3656/120024) of giants are rapid rotators, higher than the 2 per cent predicted for K giants in the field by [Carlberg et al. \(2011\)](#). For just the RC stars, the probability to be a rapid rotator $p(\text{RR}|\text{RC}) = 0.041$ (1830/44767), while for the RGB stars $p(\text{RR}|\text{RGB}) = 0.024$ (1826/75257); that is, RC stars are about twice as likely as RGB stars to be rapid rotators. However, considering only Li-rich stars, the probability to be a rapid rotator is very different, with $p(\text{RR}|\text{Li-rich,RC}) = 0.098$ (87/888) and $p(\text{RR}|\text{Li-rich,RGB}) = 0.19$ (78/418). Hence, for the Li-rich stars, the RGB stars are twice as likely as RC stars to be rapid rotators.

Considering Li richness for a given evolutionary phase and state of rotation (rapidly rotating versus non-rapidly rotating) provides more insight into the above result, since it allows us

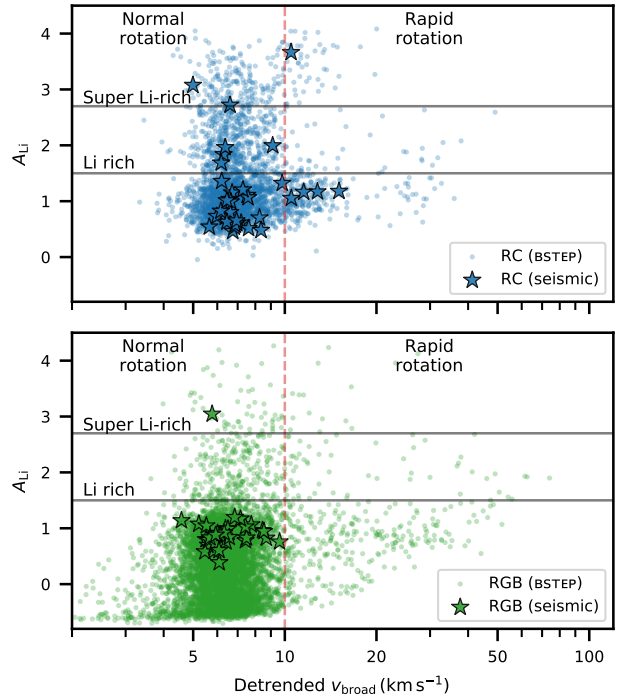


Figure 9. Using the $v_{\text{broad}}-\log g$ fit from Figure 8, for each star we calculated a detrended v_{broad} . On this scale, stars with values $> 10 \text{ km s}^{-1}$ are interpreted as rapid rotators. We show A_{Li} versus this detrended v_{broad} for the distributions of the red clump (top panel) and red giant branch (bottom panel) samples. As in Figure 4, in each panel we highlight stars asteroseismically classified as RC or RGB. RC stars are found in a smaller range of fractional v_{broad} than RGB stars, with most below 20 km s^{-1} . The rapid rotators among the Li-rich RC stars are mostly super Li-rich.

to directly investigate whether Li richness is driven by rapid rotation, and whether that depends on being an RC or an RGB star. The probability to be Li-rich for a non-rapidly-rotating star is $p(\text{Li-rich}|\text{NRR,RC}) = 0.019$ (801/42846) for an RC star, and $p(\text{Li-rich}|\text{NRR,RGB}) = 0.0046$ (340/73431) for an RGB star. However, the probability to be Li-rich for a rapidly-rotating star is much higher and is essentially equal for both RGB and RC stars: $p(\text{Li-rich}|\text{RR,RC}) = 0.048$ (87/1820), and $p(\text{Li-rich}|\text{RR,RGB}) = 0.043$ (78/1826). This indicates that in giants, rapid rotation is a mechanism for Li enrichment, and that it does not depend on the evolutionary state of a star.

In Figure 9 we explore the relationship between stellar rotation and A_{Li} . Here we plot the detrended v_{broad} , noting those stars with values $> 10 \text{ km s}^{-1}$ as rapid rotators. For both the RC and RGB populations, the Li-normal stars ($A_{\text{Li}} < 1.5$) show a range in this detrended v_{broad} , though the RC stars are more restricted, with only a few above 20 km s^{-1} . Curiously, the rapid rotators in the RC group are quite skewed toward being super Li-rich, with only a few RC stars with $1.5 < A_{\text{Li}} < 2.7$ being rapid rotators.

3.4 Spatial and orbital properties

The kinematic and chemical properties of stars in the Milky Way carry information about their origins and subsequent dynamical evolution. Kinematic substructures and mismatches between the data and a smooth distribution in an age-abundance-kinematics

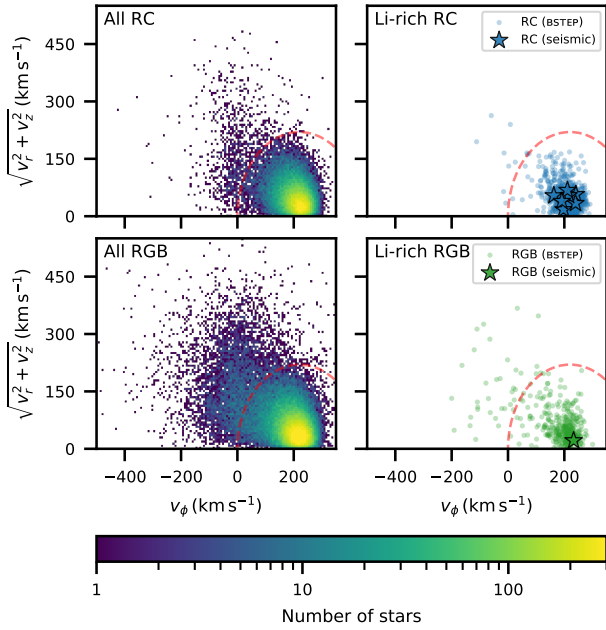


Figure 10. Galactic orbital velocities presented in the form of Toomre diagrams for (left) all stars in each sample and (right) just Li-rich stars. The top row shows RC stars; the bottom row is RGB stars. The red dashed circle on all panels indicates the region of this velocity space within which stars have disk-like orbits; stars outside of the circle have orbital velocities typical for halo stars. As expected for the GALAH survey selection, most of the stars observed have disk-like orbits, in the lithium-normal and lithium-rich groups.

space can indicate important events like minor mergers (e.g., Koppelman et al. 2018; Myeong et al. 2019; Borsato et al. 2020) and radial migration (e.g., Buder et al. 2019; Hayden et al. 2020).

The GALAH+ survey primarily samples the disk of the Milky Way, with only one per cent of the observed stars belonging to the halo (De Silva et al. 2015). The locations and metallicities of the Li-rich giants, both the RC and RGB stars, are consistent with them being mainly a disk population. This aligns well with our existing understanding of lithium-rich giants as ordinary stars.

Figure 10 shows Galactocentric rotational velocity versus perpendicular velocity (i.e., a Toomre diagram). The red circle shows the point where the total velocity relative to the Local Standard of Rest is 220 km s^{-1} , which is a canonical division between the disk and the halo (Helmi 2008). In our data set, red clump stars as a whole are more likely to be on disk-like orbits than halo-like orbits, and very few of the Li-rich RC stars are on halo-like orbits. The majority of RGB stars in our data set also orbit in the disk, but both Li-normal and Li-rich RGB stars are more likely to be on halo-like orbits than RC stars are. This is consistent with the different volumes these two sets of stars sample in a magnitude-limited survey like GALAH+.

We can further investigate the halo RGB stars in Figure 11, which shows the orbital energy E and the azimuthal action J_ϕ ($\equiv L_z$; vertical angular momentum). This is a coordinate space in which prograde orbits are on the right side of the plot and retrograde orbits are on the left. The majority of stars in our data set, which follow disk-like orbits, form the highly populated right-hand envelope of the distribution. This confirms the picture from Figure 10 that most of our Li-rich stars are found in well-behaved disk orbits — there

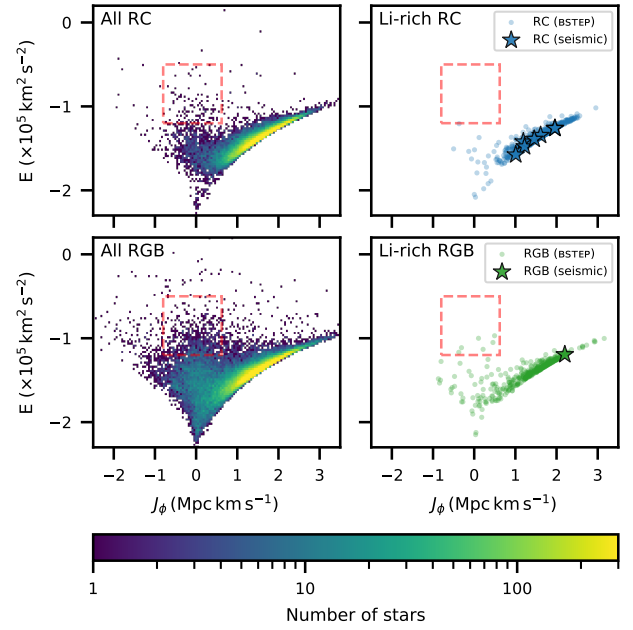


Figure 11. The J_ϕ vs orbital energy distribution for our stars, with panels arranged the same as in Figure 10. As also shown in Figure 10, the majority of our Li-rich giants have disk-like orbits — i.e., they are largely concentrated on the right edge of the envelope with low eccentricity and in-plane motions ($[-2 < E < -1] 10^5 \text{ km}^2 \text{ s}^{-2}$ and $[0 < L_z < 4] \text{ Mpc km s}^{-1}$). In all panels, the red-dashed rectangle indicates the region of parameter space where stars from the Gaia-Enceladus merger event are found (Koppelman et al. 2018). A handful of our Li-rich RGB stars fall into this box, and a more detailed investigation to chemically and kinematically tag these stars to the Gaia-Enceladus merger event is planned.

are few Li-rich giants in orbits with high energy relative to their angular momentum, or with nonrotating or retrograde orbits.

The dashed red rectangle in Figure 11 highlights the region of this parameter space occupied by the remnant of the Gaia-Enceladus merger event (Helmi et al. 2018; Koppelman et al. 2018). A handful of the Li-rich stars in our data set are located in this region of kinematic space. The recent study of Molaro et al. (2020) investigates the overall behaviour of lithium and beryllium in stars kinematically consistent with Gaia-Enceladus. The authors find that the overall evolution of lithium abundance is similar to the chemical evolution pattern in the Milky Way, suggesting that the Spite Plateau (Spite & Spite 1982) is a universal upper limit for lithium abundance in low-mass stars and is not a special feature of the Milky Way. Only one of the 101 stars in that study is Li-rich, which matches the 1% occurrence rate we find in our overall sample.

A more detailed investigation to chemically and kinematically tag the stars in our data set to the Gaia-Enceladus merger event would be required to positively identify them as having an extragalactic origin.

3.5 Binarity

Recent works have presented two models involving binary stars to explain lithium enrichment on the red clump. Casey et al. (2019) used a large set of Li-rich giants from the LAMOST survey to argue that the distribution of Li-rich giants in evolutionary phase requires independent processes operating on the first-ascendant

branch and after the helium flash, based on the lithium depletion timescale in stellar atmospheres. Their proposed mechanism in red clump stars is tidal spin-up from a binary companion driving internal mixing and therefore lithium production via the [Cameron & Fowler \(1971\)](#) mechanism. In contrast, [Zhang et al. \(2020\)](#) proposed that Li-rich RC stars are the result of mergers in RGB-white dwarf binary systems.

These hypotheses are in principle testable by searching for binary companions (or lack thereof) in Li-rich giants through variability in radial velocity, photometry and astrometry. Unfortunately, as we discuss in this subsection, we are not able to draw any significant conclusions on binarity in our data set from radial velocity, photometry, or astrometry. Recent work by [Travençolo et al. \(2020\)](#) analyzed the GALAH survey spectra to identify spectroscopic binary stars, and found a handful of RC binaries, including a few that were lithium rich. Follow-up work to re-derive the lithium abundances of the individual stars could be quite useful in understanding how important binary RC stars are in the family of lithium-rich giants.

For the representative binary of [Casey et al. \(2019\)](#) — a 1.5 solar mass giant and a 1.0 solar mass dwarf in a 279-day orbit — there are some observable spectroscopic and photometric signatures. We would expect radial velocity variations on the order of $\sim 30 \text{ km s}^{-1}$ (as modelled by `ELLIC`; [Maxted 2016](#)). This is well within the precision of HERMES but we do not have the necessary observational cadence to confidently identify these periodic variations. [Price-Whelan et al. \(2020b\)](#) identified 19,635 candidate binaries in the APOGEE survey based on radial velocity variations between multiple observations. Of these 66 were in our GALAH+DR3 giant star data set, including 20 of our RC stars — one of which is Li-rich. It has only three observations with APOGEE, indicating an RV range of $\sim 50 \text{ km s}^{-1}$.

In terms of photometric signatures of binarity in the form of transits, assuming random orbital inclinations and observed orbital period distributions (e.g., [Raghavan et al. 2010](#)), 2.5 ± 0.5 per cent of our Li-rich RC stars should be in eclipsing binary systems. The secondary star will block about 1 per cent of the disk of the primary with an eclipse period of ~ 3 days. This does not require a very high cadence in photometric monitoring, but none of our Li-rich RC stars have so far had light curves in ASAS-SN ([Kochanek et al. 2017](#)) or *TESS* ([Ricker et al. 2014](#)) that show evidence for eclipses.

The astrometry from *Gaia* is precise enough to measure the motion of the photocentre of some binary systems (depending on heliocentric distance and the binary properties). The model assumption underlying the data processing for *Gaia* DR2 is that sources are single objects, and if there are photocentre shifts in binary systems these are interpreted as larger than expected astrometric errors. Work by [Penoyre et al. \(2020\)](#) and [Belokurov et al. \(2020\)](#) have used large values of the Renormalized Unit Weight Error (RUWE), an astrometric error metric reported by *Gaia*, to identify possible binaries. Our data set excludes stars with large RUWE by construction (it is part of `flag_sp`), because parallax is an important prior in our stellar parameter determination.

3.6 Infrared excess

A fraction of Li-rich RGB stars have been reported to have excess flux in their spectral energy distribution in the infrared, which has been postulated as a sign of a physical connection between lithium production and mass loss. This can be seen in photometry from the *IRAS* satellite (e.g., [Fekel & Watson 1998](#)) and from *WISE*, although the latter’s wavelength coverage does not reach as far into the infrared. A close investigation by [Rebull et al. \(2015\)](#) found that

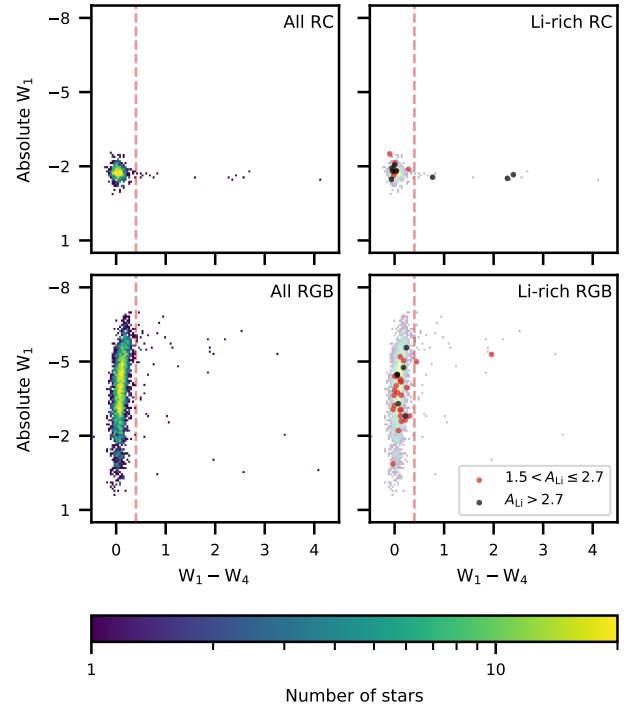


Figure 12. The infrared colour-magnitude diagram for stars in our data set with reliable *WISE* photometry, showing (top row) RC stars, (bottom row) RGB stars, and (left column) all stars in each sample and (right column) just Li-rich stars. Stars to the right of vertical line at $W_1 - W_4 = 0.5$ are interpreted as having an infrared excess. The majority of stars show no such excess, but there are a handful of stars that do. The proportion of IR excess stars that are Li-rich (5/69; 7 per cent) is higher than the proportion of the general population of giants that are Li-rich (42/4300; 1 per cent).

the majority of lithium-rich giants in the literature with reported infrared excesses were artifacts in the *WISE* catalog or cases of source confusion. However, they do confirm some as real cases of infrared excess, and they do find that the stars with the largest infrared excess are lithium-rich K giants.

Within our data set (Figure 12), there are only 4349 giants with clean *WISE* detections; that is, they have the `cc_flags` confusion flag set to `0000` and the `ph_qual` photometric quality flag set to `A` for W_1 and W_4 . These can be divided into 764 RC stars (15 of which are Li-rich) and 3585 RGB stars (31 Li-rich). Overall only a few stars have large infrared colours (defined as $W_1 - W_4 > 0.5$): 16 of the RC stars and 53 of the RGB stars. Of the 46 Li-rich giants with useful *WISE* photometry, five have large infrared colours. Two of these are RGB stars located high on the giant branch. The other three have been classified as RC stars, and all three of those are super Li-rich.

The probability to be Li-rich is higher for giants with infrared excess (5/69; 7 per cent) as compared to giants without infrared excess (42/4300; 1 per cent), but the statistical significance of this result is low due to the small sample size. Considering just the RC stars with infrared excess, 3/16 are Li-rich, while 2/53 RGB stars with IR excess are Li-rich.

In our data set, the stars with the largest infrared colours are located on the upper RGB and at the RC. Infrared excess and mass loss are related, since the upper RGB is the stage at which the star’s atmosphere is extended, cool, and likely to be lost. The red

clump is the immediate next step in stellar evolution, and so it is reasonable that we find RC stars that appear to have surrounding material lost during the late RGB, and that infrared excess is more closely tied to Li enrichment in RC stars than in RGB stars. However, it remains unclear what the mechanism connecting mass loss and lithium enrichment would be in stars on their first ascent of the giant branch.

3.7 Super lithium-rich stars

In our discussion and figures so far we have been making a distinction between lithium-rich stars, which have $A_{\text{Li}} > 1.5$, and super lithium-rich stars, which sit above the primordial abundance of $A_{\text{Li}} = 2.7$. This is an important distinction for any model of lithium enrichment that involves adding pristine gas to an evolved star to raise its abundance, because that process can only raise a star's abundance toward the initial abundance in that gas but could not exceed it.

For lithium enrichment models that require the production of lithium within a star, this distinction is less important, but the question of how to produce the observed amount of lithium is more difficult to answer at higher abundance. Yan et al. (2018) attempt to model the process for lithium production in the star TYC 429-2097-1, which has an abundance of $A_{\text{Li}} = 4.5$. They find that meridional circulation at the RGB bump, the current evolutionary stage of this star, is capable of producing more than the observed amount of lithium. The most lithium-rich giant in our data set also has $A_{\text{Li}} = 4.5^3$, but as a luminous giant (see Table 1 and Figure 4) it does not fit within their model.

Super lithium-rich red clump stars in our data set have some interesting properties. While the majority of our super lithium-rich stars are in the red clump phase (Section 2.4), almost none of them are on the secondary red clump, indicating a connection between stellar mass and the ability to produce large amounts of lithium. Exploring this mass dependence with precise masses would be extremely useful future work. While the super Li-rich red clump stars are the most rapidly rotating (Fig. 8) and the most metal-rich (Fig. 6), these two groups of super Li-rich red clump stars are not the same set of stars: the most metal-rich RC stars are not rapidly rotating.

3.8 Summary of observational phenomenology

In this study we explore the properties of 1306 evolved stars from the GALAH+ survey with elevated photospheric abundances of lithium ($A_{\text{Li}} > 1.5$). We find these main behaviours in the data set:

- (i) Red clump stars are more than three times as likely to be lithium rich as red giant branch stars (Section 2.4).
- (ii) The less massive primary RC stars are much more likely than the more massive secondary RC stars to be super lithium-rich (Section 2.4).
- (iii) The occurrence rate of lithium-rich giants with metallicity is markedly different for RC and RGB populations: it increases steadily with metallicity in red clump stars, but it is essentially constant in red giant branch stars below solar metallicity and increases sharply thereafter (Section 3.1).

³ See Section 2.3 for discussion about our inability to identify stars with $A_{\text{Li}} > 4.6$.

(iv) Rapidly rotating stars are much more likely to be Li-rich than non-rotating stars, but the probability of a star to be Li-rich given that it is rapidly rotating is same for RGB and RC stars. This indicates that rapid rotation is a mechanism for Li enrichment in giants that is independent of evolutionary phase (Section 3.3).

(v) Rapidly rotating lithium-rich RC stars tend to be super lithium-rich (Section 3.3).

We recover the changing occurrence rate of lithium-rich giants with metallicity noted by Casey et al. (2019) and Deepak et al. (2020). We do find a smaller fraction of our Li-rich giants to be RC stars than in Casey et al. (2019), 68 per cent versus their 80^{+7}_{-6} per cent. However, without a precise description of their method for classifying RC vs RGB stars, it is difficult to know to what extent this disagreement is a result of the RC versus RGB classification, the difference in abundance accuracy and precision in the two studies, or the difference between the GALAH and LAMOST selection functions.

Both rapid rotation and infrared excess show some connection to lithium enrichment, in that stars with those properties are more likely to be lithium-rich than stars without them. However, the majority of lithium-rich stars do not exhibit either of these features. As also observed by Zhou et al. (2019), Li-rich stars with infrared excess are not the same Li-rich stars as those that are rapid rotators.

4 THE ORIGINS OF LITHIUM ENRICHMENT IN EVOLVED STARS

The broad strokes of the proposed explanations for how a small fraction of evolved stars have come to be enriched in lithium have not changed substantially since the first lithium-rich giant was identified by McKellar (1940). Models invoke either some external reservoir of lithium (ingestion of a planet or sub-stellar companion; or mass transfer from an AGB companion) or some internal production channel (internal mixing driven by the RGB bump phase, the He flash, rotation, or binary interactions). The consensus from observational studies, especially those with large data sets, is that there must be multiple processes at work to create the combination of RGB bump stars, luminous giants, and red clump stars we find with enhanced lithium abundances.

The correspondence in red clump stars between rapid rotation and the highest levels of lithium enrichment implies quite strongly that rotationally driven mixing processes are capable of driving lithium production. However, the fraction of rapidly rotating stars that are Li-rich is 4 to 5 per cent for both the RC and the RGB, indicating that rotationally driven mixing is not the only process at work. Asteroseismology presents an opportunity to measure the internal rotation of RGB stars that have rotational axes aligned appropriately to the line of sight (e.g., Mosser et al. 2012; Deheuvels et al. 2012). Studies of additional Li-rich giants in the Kepler field and the TESS continuous viewing zone would be very helpful in understanding whether there is a connection between core rotation and lithium enrichment.

For stars on the red giant branch, we find that there is a concentration of Li-rich stars near the RGB bump, which can be explained as a result of internal mixing triggered by a change in internal structure. We also find Li-rich stars at all luminosities and metallicities on the RGB. The occurrence rate for Li-rich RGB stars is essentially constant for all subsolar metallicities and dramatically higher at supersolar metallicity. This suggests either two independent lithium enrichment processes for RGB stars, or one process that is strongly suppressed at low metallicity. It is unclear how compatible

a metallicity-independent lithium enrichment process on the RGB is with planet engulfment models, since the planet occurrence rate for gas giants is not a straightforward function of metallicity. Further abundance studies focused on boron and beryllium could shed some light on this problem, since they have similar burning temperatures to lithium and should be also be enriched during planet engulfment (e.g., see initial work by Drake et al. 2017; Carlberg et al. 2018). Planet engulfment is expected to result in a different ratio of ${}^6\text{Li}/{}^7\text{Li}$ compared to internal lithium production processes, but measuring this will be observationally challenging (Aguilera-Gómez et al. 2020).

As in previous studies, the majority of our lithium-rich giants are red clump stars, and this requires a lithium enrichment process triggered at, or after, the helium flash. The fact that the occurrence rate for RC stars rises steadily with increasing metallicity may be a result of the fact that the time spent on the red clump is longer at higher metallicity, or it may reflect a more effective internal mixing in high metallicity giant stars because of their less compressed interior structure, or it may be driven by a higher binary fraction (with the correct mass ratio and orbital separation) at higher metallicity. These possibilities will need to be evaluated through careful modeling of stellar structure, evolution, and star formation. With the present data set we cannot comment directly on binary interactions as the driver for internal mixing, but this is an avenue for future work that may clarify the situation significantly.

ACKNOWLEDGEMENTS

SLM and AGB acknowledge support from the UNSW Scientia Fellowship program, and SLM and JDS acknowledge support from the Australian Research Council through Discovery Project grant DP180101791. SB acknowledges funds from the Alexander von Humboldt Foundation in the framework of the Sofja Kovalevskaja Award endowed by the Federal Ministry of Education and Research. Y.S.T. is grateful to be supported by the NASA Hubble Fellowship grant HST-HF2-51425.001 awarded by the Space Telescope Science Institute. Parts of this research were conducted by the Australian Research Council Centre of Excellence for All Sky Astrophysics in 3 Dimensions (ASTRO 3D), through project number CE170100013.

This work is based on data acquired through the Anglo-Australian Telescope, under programmes: The GALAH survey (A/2013B/13, A/2014A/25, A/2015A/19, A/2017A/18); The K2-HERMES K2 follow-up program (A/2015A/03, A/2015B/19, A/2016A/22, A/2016B/12, A/2017A/14); The TESS-HERMES program (A/2016B/10); Accurate physical parameters of *Kepler* K2 planet search targets (A/2015B/01); Planets in clusters with K2 (S/2015A/012). We acknowledge the traditional owners of the land on which the AAT stands, the Gamilaraay people, and pay our respects to elders past and present.

This work has made use of data from the European Space Agency (ESA) mission *Gaia* (<https://www.cosmos.esa.int/gaia>), processed by the *Gaia* Data Processing and Analysis Consortium (DPAC, <https://www.cosmos.esa.int/web/gaia/dpac/consortium>). Funding for the DPAC has been provided by national institutions, in particular the institutions participating in the *Gaia* Multilateral Agreement.

This paper includes data collected by the K2 mission. Funding for the K2 mission is provided by the NASA Science Mission directorate.

This publication makes use of data products from the Wide-field Infrared Survey Explorer, which is a joint project of the Uni-

versity of California, Los Angeles, and the Jet Propulsion Laboratory/California Institute of Technology, funded by the National Aeronautics and Space Administration.

The following software and programming languages made this research possible: ASTROPY (v4.0.1; Astropy Collaboration et al. 2018); ELLC (1.8.5; Maxted 2016); GALA (v1.1; Price-Whelan et al. 2020a); H5PY (v2.10.0); MATPLOTLIB (v3.1.3; Hunter 2007; Caswell et al. 2020); MPL_SCATTER_DENSITY; PYTHON (v3.8.3); SEABORN (v0.10.1; Waskom et al. 2020); SCIPY (v1.4.1; SciPy 1.0 Contributors et al. 2020); TOPCAT (v4.7 Taylor 2005, 2006).

References

- Aguilera-Gómez C., Chanamé J., Pinsonneault M. H., Carlberg J. K., 2016, *ApJ*, 829, 127
- Aguilera-Gómez C., Chanamé J., Pinsonneault M. H., 2020, preprint ([arXiv:2005.14209](https://arxiv.org/abs/2005.14209))
- Angelou G. C., D’Orazi V., Constantino T. N., Church R. P., Stancliffe R. J., Lattanzio J. C., 2015, *MNRAS*, 450, 2423
- Asplund M., Grevesse N., Sauval A. J., Scott P., 2009, *ARA&A*, 47, 481
- Astropy Collaboration et al., 2018, *AJ*, 156, 123
- Bailer-Jones C. A. L., Rybizki J., Foesneau M., Mantelet G., Andrae R., 2018, *AJ*, 156, 58
- Bedding T. R., et al., 2011, *Nature*, 471, 608
- Belokurov V., et al., 2020, *MNRAS*
- Borsato N. W., Martell S. L., Simpson J. D., 2020, *MNRAS*, 492, 1370
- Buder S., et al., 2018, *MNRAS*, 478, 4513
- Buder S., et al., 2019, *A&A*, 624, A19
- Burbidge E. M., Burbidge G. R., Fowler W. A., Hoyle F., 1957, *Reviews of Modern Physics*, 29, 547
- Cameron A. G. W., Fowler W. A., 1971, *ApJ*, 164, 111
- Carlberg J. K., Majewski S. R., Patterson R. J., Bizyaev D., Smith V. V., Cunha K., 2011, *ApJ*, 732, 39
- Carlberg J. K., Cunha K., Smith V. V., Majewski S. R., 2012, *ApJ*, 757, 109
- Carlberg J., Cunha K., Smith V., do Nascimento J., 2018, in *The 20th Cambridge Workshop on Cool Stars*. Zenodo, Boston, MA, [doi:10.5281/zenodo.1489212](https://doi.org/10.5281/zenodo.1489212)
- Carney B. W., Latham D. W., Stefanik R. P., Laird J. B., 2008a, *AJ*, 135, 196
- Carney B. W., Gray D. F., Yong D., Latham D. W., Manset N., Zelman R., Laird J. B., 2008b, *AJ*, 135, 892
- Casey A. R., et al., 2016, *MNRAS*, 461, 3336
- Casey A. R., et al., 2019, *ApJ*, 880, 125
- Caswell T. A., et al., 2020, *Matplotlib/Matplotlib v3.1.3*, Zenodo, [doi:10.5281/ZENODO.3633844](https://doi.org/10.5281/ZENODO.3633844)
- Charbonnel C., Balachandran S. C., 2000, *A&A*, 359, 563
- Cui X.-Q., et al., 2012, *Research in Astronomy and Astrophysics*, 12, 1197
- Cybert R. H., Fields B. D., Olive K. A., 2008, *J. Cosmology Astropart. Phys.*, 2008, 012
- De Silva G. M., et al., 2015, *MNRAS*, 449, 2604
- Deepak Reddy B. E., 2019, *MNRAS*, 484, 2000
- Deepak Lambert D. L., Reddy B. E., 2020, *MNRAS*, 494, 1348
- Deheuvels S., et al., 2012, *ApJ*, 756, 19
- Denissenkov P. A., 2012, *ApJ*, 753, L3
- Drake N. A., de la Reza R., Smith V. V., Cunha K., 2017, *Proceedings of the International Astronomical Union*, 13, 237
- Fekel F. C., Watson L. C., 1998, *AJ*, 116, 2466
- Fields B. D., Olive K. A., Yeh T.-H., Young C., 2020, *J. Cosmology Astropart. Phys.*, 2020, 010
- Gaia Collaboration et al., 2016, *A&A*, 595, A1
- Gaia Collaboration et al., 2018, *A&A*, 616, A1
- Gamow G., Landau L., 1933, *Nature*, 132, 567
- Gao Q., Shi J.-R., Yan H.-L., Yan T.-S., Xiang M.-S., Zhou Y.-T., Li C.-Q., Zhao G., 2019, *ApJS*, 245, 33
- Gilmore G., et al., 2012, *The Messenger*, 147, 25
- Girardi L., 2016, *ARA&A*, 54, 95

- Gonzalez O. A., et al., 2009, *A&A*, 508, 289
- Gratton R. G., Sneden C., Carretta E., Bragaglia A., 2000, *A&A*, 354, 169
- Gustafsson B., Edvardsson B., Eriksson K., Jørgensen U. G., Nordlund Å., Plez B., 2008, *A&A*, 486, 951
- Hansen T. T., Andersen J., Nordström B., Beers T. C., Placco V. M., Yoon J., Buchhave L. A., 2016, *A&A*, 588, A3
- Hawkins K., Ting Y.-S., Walter-Rix H., 2018, *ApJ*, 853, 20
- Hayden M. R., et al., 2020, *MNRAS*, 493, 2952
- Helmi A., 2008, *A&ARv*, 15, 145
- Helmi A., Babusiaux C., Koppelman H. H., Massari D., Veljanoski J., Brown A. G. A., 2018, *Nature*, 563, 85
- Hon M., Stello D., Yu J., 2018, *MNRAS*, 476, 3233
- Hunter J. D., 2007, *Computing in Science & Engineering*, 9, 90
- Iben I., 1965, *ApJ*, 142, 1447
- Kallinger T., et al., 2012, *A&A*, 541, A51
- Karaali S., Bilir S., Gokce E. Y., Plevne O., 2019, *PASA*, 36, e040
- Karakas A. I., Lugaro M., 2016, *ApJ*, 825, 26
- Kirby E. N., Fu X., Guhathakurta P., Deng L., 2012, *ApJ*, 752, L16
- Kirby E. N., Guhathakurta P., Zhang A. J., Hong J., Guo M., Guo R., Cohen J. G., Cunha K., 2016, *ApJ*, 819, 135
- Kochanek C. S., et al., 2017, *PASP*, 129, 104502
- Koppelman H., Helmi A., Veljanoski J., 2018, *ApJ*, 860, L11
- Kos J., et al., 2017, *MNRAS*, 464, 1259
- Kraft R. P., Peterson R. C., Guhathakurta P., Sneden C., Fulbright J. P., Langer G. E., 1999, *ApJ*, 518, L53
- Lagarde N., et al., 2019, *A&A*, 621, A24
- Lewis I. J., et al., 2002, *MNRAS*, 333, 279
- Lind K., Primas F., Charbonnel C., Grundahl F., Asplund M., 2009, *A&A*, 503, 545
- Mainzer A., et al., 2011, *ApJ*, 731, 53
- Marigo P., et al., 2017, *ApJ*, 835, 77
- Martell S. L., Shetrone M. D., 2013, *MNRAS*, 430, 611
- Martell S. L., et al., 2017, *MNRAS*, 465, 3203
- Maxted P. F. L., 2016, *A&A*, 591, A111
- McKellar A., 1940, *PASP*, 52, 407
- McKellar A., 1941, *The Observatory*, 64, 4
- Molaro P., Cescutti G., Fu X., 2020, preprint ([arXiv:2006.00787](https://arxiv.org/abs/2006.00787))
- Mosser B., et al., 2012, *A&A*, 548, A10
- Myeong G. C., Vasiliev E., Iorio G., Evans N. W., Belokurov V., 2019, *MNRAS*, 488, 1235
- Penoyre Z., Belokurov V., Evans N. W., Everall A., Koposov S. E., 2020, *MNRAS*, 495, 321
- Pilachowski C. A., Sneden C., Kraft R. P., Harmer D., Willmarth D., 2000, *AJ*, 119, 2895
- Piskunov N., Valenti J. A., 2017, *A&A*, 597, A16
- Plevne O., Önal Taş Ö., Bilir S., Seabroke G. M., 2020, *ApJ*, 893, 108
- Price-Whelan A., Sipőcz B., Lenz D., Greco J., Major S., Koposov S., Oh S., Lim P. L., 2020a, *Adrn/Gala: V1.1*, Zenodo, [doi:10.5281/ZENODO.3700827](https://doi.org/10.5281/ZENODO.3700827)
- Price-Whelan A. M., et al., 2020b, *ApJ*, 895, 2
- Raghavan D., et al., 2010, *ApJS*, 190, 1
- Ramírez I., Fish J. R., Lambert D. L., Allende Prieto C., 2012, *ApJ*, 756, 46
- Rebull L. M., et al., 2015, *AJ*, 150, 123
- Ricker G. R., et al., 2014, *Journal of Astronomical Telescopes, Instruments, and Systems*, 1, 014003
- Salpeter E. E., 1955, *Physical Review*, 97, 1237
- SciPy 1.0 Contributors et al., 2020, *Nature Methods*
- Sharma S., et al., 2018, *MNRAS*, 473, 2004
- Sharma S., et al., 2019, *MNRAS*, 490, 5335
- Sheinis A., et al., 2015, *Journal of Astronomical Telescopes, Instruments, and Systems*, 1, 035002
- Silva Aguirre V., et al., 2020, *ApJ*, 889, L34
- Singh R., Reddy B. E., Bharat Kumar Y., Antia H. M., 2019, *ApJ*, 878, L21
- Smiljanic R., et al., 2018, *A&A*, 617, A4
- Spite M., Spite F., 1982, *Nature*, 297, 483
- Stassun K. G., et al., 2019, *AJ*, 158, 138
- Stello D., et al., 2013, *ApJ*, 765, L41
- Stello D., et al., 2017, *ApJ*, 835, 83
- Taylor M. B., 2005, in Shopbell P., Britton M., Ebert R., eds, Vol. 347, ADASS XIV ASP Conference Series. Astronomical Society of the Pacific, San Francisco, USA, p. 29
- Taylor M. B., 2006, in Gabriel C., Arviset C., Ponz D., Enrique S., eds, ASP Conference Series Vol. 351, ADASS XV. Astronomical Society of the Pacific, San Francisco, CA, p. 666
- Traven G., et al., 2020, preprint ([arXiv:2005.00014](https://arxiv.org/abs/2005.00014))
- Trimble V., 1975, *Reviews of Modern Physics*, 47, 877
- Trimble V., 1991, *A&ARv*, 3, 1
- Valenti J. A., Piskunov N., 1996, *A&AS*, 118, 595
- Vrard M., Mosser B., Samadi R., 2016, *A&A*, 588, A87
- Wallerstein G., Conti P. S., 1969, *ARA&A*, 7, 99
- Wallerstein G., Sneden C., 1982, *ApJ*, 255, 577
- Waskom M., et al., 2020, *Mwaskom/Seaborn: V0.10.1* (April 2020), Zenodo, [doi:10.5281/ZENODO.3767070](https://doi.org/10.5281/ZENODO.3767070)
- Wittenmyer R. A., et al., 2018, *AJ*, 155, 84
- Wright E. L., et al., 2010, *AJ*, 140, 1868
- Yan H.-L., et al., 2018, *Nature Astronomy*, 2, 790
- Zhang X., Jeffery C. S., Li Y., Bi S., 2020, *ApJ*, 889, 33
- Zhou Y., et al., 2019, *ApJ*, 877, 104

This paper has been typeset from a $\text{\TeX}/\text{\LaTeX}$ file prepared by the author.